Superconducting correlations induced by charge ordering in cuprate superconductors and Fermi-arc formation

E. V. L. de Mello[1,*] and J. E. Sonier[2,3]

[1]*Instituto de Física, Universidade Federal Fluminense, 24210-346 Niterói, RJ, Brazil*

[2]*Department of Physics, Simon Fraser University, Burnaby, British Columbia V5A 1S6, Canada*

[3]*Canadian Institute for Advanced Research, Toronto, Ontario M5G 1Z8, Canada*

(Received 19 January 2017; revised manuscript received 27 March 2017; published 30 May 2017)

We have developed a generalized electronic phase separation model of high-temperature cuprate superconductors that links the two distinct energy scales of the superconducting (SC) and pseudogap (PG) phases via a charge-density-wave (CDW) state. We show that simulated electronic-density modulations resembling the charge order modulations detected in cuprates intertwine the SC and charge orders by localizing charge and providing the energy scale for a spatially periodic SC attractive potential. Bulk superconductivity is achieved with the inclusion of Josephson coupling between nanoscale domains of intertwined fluctuating CDW and SC orders, and local SC phase fluctuations give rise to the Fermi arcs along the nodal directions of the SC gap. We demonstrate the validity of the model by reproducing the hole-doping dependence of the PG onset temperature T^*, and the SC transition temperature T_c of $YBa_2Cu_3O_y$ and $Bi_{2-y}Pb_ySr_{2-z}La_zCuO_{6+\delta}$. The results show that the periodicity of the CDW order is controlled by the PG energy scale, and the hole-doping dependence of the SC energy gap is controlled by the charge ordering.

DOI: 10.1103/PhysRevB.95.184520

I. INTRODUCTION

Experiments using different methods have established the occurrence of short-range, incommensurate static charge-density-wave (CDW) correlations in a variety of high-temperature superconducting (SC) cuprates [1–18]. With the exception of La-based cuprates in which CDW order is accompanied by spin order, the charge order (CO) observed in different cuprate families appears to be similar. In zero magnetic field, the CDW order is essentially two dimensional. The wave vector of the CDW order is parallel to the Cu-O bond directions along the a and b axes, and decreases in magnitude with increased charge doping. While much of the experimental data cannot distinguish between checkerboard (bidirectional) or alternating stripe (unidirectional) CO, resonant x-ray scattering (RXS) experiments on underdoped $YBa_2Cu_3O_7$ (Y123) [7] and an analysis of scanning tunneling microscopy (STM) data for $Bi_2Sr_2CaCu_2O_{8+\delta}$ [19] indicate that the inter-unit-cell character is one of segregated or overlapping unidirectional charge-ordered stripes. Furthermore, it has been found that the CDW order possesses a d-wave intra-unit-cell symmetry with the modulated charge primarily on the O-2p orbitals linking the Cu atoms [8–10]. Since the SC order parameter also has d-wave symmetry, this local charge or bond order symmetry supports theoretical proposals that suggest the charge and SC order parameters are intimately intertwined. Some attribute the d-wave CO symmetry to quasiparticle scattering by antiferromagnetic (AF) fluctuations near a metallic quantum critical point, which also gives rise to the d-wave superconductivity [20–22]. Alternatively, it has been proposed that CDW order in cuprates is a consequence of a pair-density wave (PDW) phase, in which the SC order parameter is periodically modulated in space due to the Cooper pairs having finite momentum [23–26].

The aim of our work is to establish a quantitative link between the inter-unit-cell dependence of the CO resolved by RXS and imaged in real space by STM, and the energy gaps of the pseudogap (PG) and SC phases. Our model is based on an intrinsic propensity for mesoscale electronic phase separation below an onset temperature T_{PS} that follows the hole-doping dependence of the PG temperature T^*. This picture is similar to that previously advocated by Fradkin and Kivelson [27]. We presume the onset of fluctuating CDW order domains at T^*, where STM measurements on $Bi_2Sr_2CaCu_2O_{8+\delta}$ have detected the emergence of charge stripes that extend into the overdoped regime [28]. The short-range static CO that has been observed by x rays at a lower temperature $T_{CO} \leqslant T^*$ is assumed to be confined to local regions where fluctuating CDW order has become pinned by disorder. Contrary to this assumption, we note that in $HgBa_2CuO_{4+\delta}$ (Hg1201) CDW order observed by x-ray scattering vanishes already well below optimal doping [18]. This seems to be due to the presence of pairs of interstitial oxygens within the same unit cell specific to Hg1201. Although not captured by our model, it is also important to recognize that the PG region marks the onset of an intra-unit-cell magnetic order [29,30], a true phase transition that modifies ultrasonic waves [31], an increase in antiferromagnetic correlations [32] and global inversion-symmetry breaking [33].

Another important ingredient of our model is the experimental observation that the CDW periodicity is independent of temperature, leading us to surmise that the CDW periodicity is set by the onset of the PG at T^*. This implies that the CDW order is a consequence of the PG formation. At low doping ($p \leqslant 0.12$) where T_{CO} decreases with decreasing doping, CDW order is potentially suppressed by a slowing down of spin fluctuations and a tendency toward static SDW order. Compatible with experimental signatures of pairing or SC correlations persisting above T_c [34–40], our model shows that CDW order in the PG regime may induce SC domains that grow and connect to establish bulk superconductivity at T_c.

*Corresponding author: evandro@if.uff.br

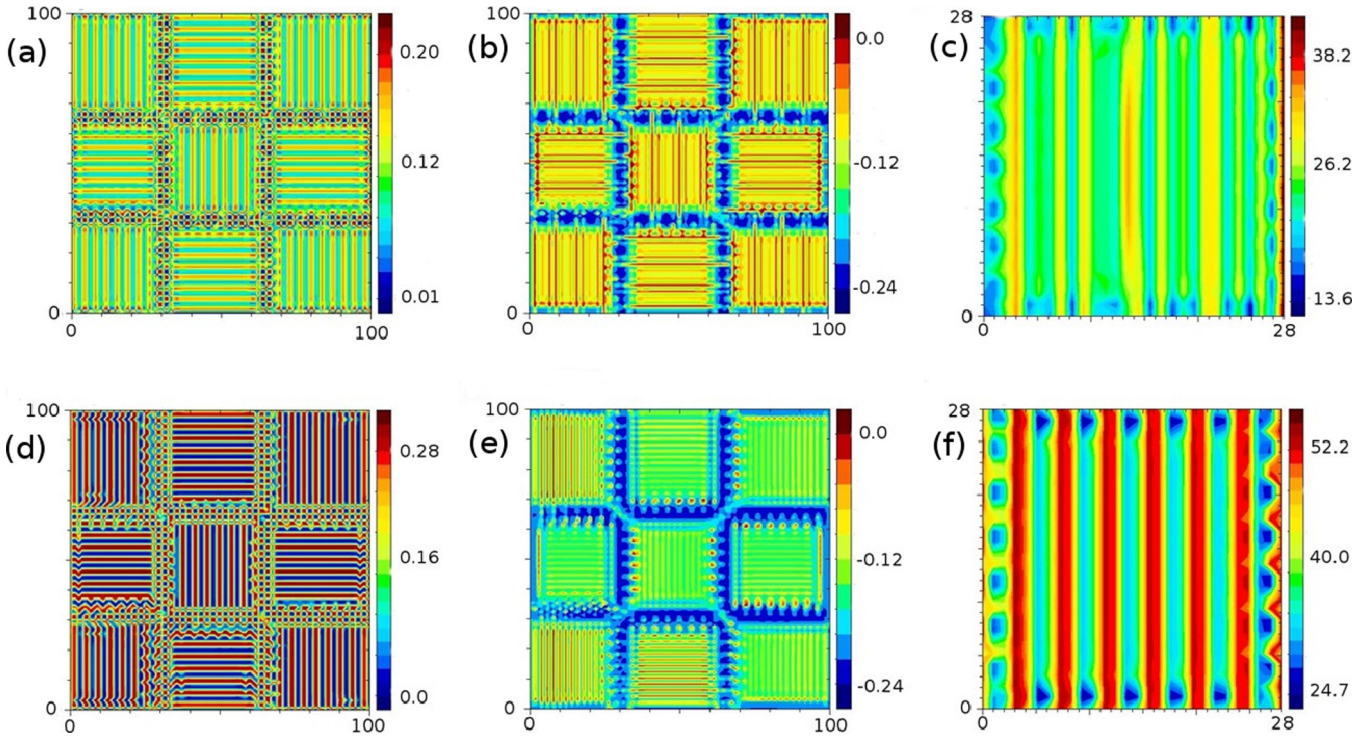

FIG. 1. Contour plots of the electronic density $p(\mathbf{r})$ calculated on a square lattice of 100×100 unit cells, with average charge densities of $p = 0.12$ in (a) and $p = 0.16$ in (d). The charge order wavelengths are $\lambda_{CO} = 3.15a_0$ (a) and $\lambda_{CO} = 3.49a_0$ in (d), corresponding to the charge order wave vectors determined by momentum-resolved x-ray probes [4,5,7]. (b), (e) Corresponding spatial dependence of the free-energy potential $V_{GL}(\mathbf{r})$. The periodicity of the potential manifests in the periodic modulations of the charge density. (c), (f) Results of calculations of the d-wave pairing potential $\Delta_d(\mathbf{r})$ displayed for a single domain over a 28×28 unit cell area (in meV unit). The spatial average value of the pair potential $\langle \Delta_d(\mathbf{r}) \rangle$ is 25.5 meV at $p = 0.12$ in (c), and 43.8 meV at $p = 0.16$ in (f).

II. SIMULATION OF THE CHARGE-ORDERED STATE

Our approach is to first simulate spatial modulations of the electronic structure resembling experimentally resolved inter-unit-cell CO modulations, using the time-dependent Cahn-Hilliard (CH) differential equation [41]. Besides generating the desired CDW order, the CH approach yields the associated free-energy modulations, which we assume scales with a periodic attractive potential in the subsequent SC calculations. The starting point is the introduction of a time-dependent conserved order parameter associated with the local electronic density, $u(\mathbf{r},t) = [p(\mathbf{r},t) - p]/p$, where p is the average charge density and $p(\mathbf{r},t)$ is the charge density at a position $\mathbf{r}$ in the plane. The Ginzburg-Landau (GL) free-energy density of the system is of the form

$$f(u) = \tfrac{1}{2}\varepsilon|\nabla u|^2 + V_{GL}(u,T), \qquad (1)$$

where $V_{GL}(u,T) = -\alpha[T_{PS} - T]u^2/2 + B^2u^4/4 + \ldots$ is a double-well potential that characterizes the electronic phase separation below T_{PS}. The parameters α and B are constants, and ε controls the spatial separation of the charge-segregated patches. The CH equation obtained from the continuity equation for the local free-energy current density $\mathrm{J} = -\mathrm{M}\nabla\mu$ (where M is the charge mobility and $\mu = \partial f/\partial\mu$ is the chemical potential) is given by Eq. (A1). Demonstrative solutions of this equation (i.e., charge order simulations) are displayed in Appendix A. For each time step the CH equation is solved for $u(\mathbf{r},t)$, and $p(\mathbf{r},t)$ is obtained. We adjust the parameters of the free energy such that when the periodicity of $p(\mathbf{r},t)$ matches that of the experimentally observed CDW order, the calculation is stopped and the solution is taken to be the spatially dependent static electronic density $p(\mathbf{r})$. Since the method described here does not generate an intra-unit-cell CO symmetry, it is applicable to systems that have SC pairing and CO symmetries other than d-wave.

Figure 1(a) shows a simulation of alternating planar domains of 90°-rotated charge stripes with an intra-domain periodicity compatible with RXS data for detwinned Y123 at $p = 0.12$ [8]. Within each domain the CO wavelength is $\lambda_{CO} = 3.15a_0$, where the in-plane lattice constant is $a_0 = 3.85$ Å. The CO wavelength in Y123 measured by various x-ray methods increases with increased hole doping [4,5,42]. We have used such data to generate similar CO striped patterns for Y123 at $p = 0.16$ [Fig. 1(d)] and $p = 0.09$.

STM differential conductance maps for optimally doped ($T_c = 35$ K) and underdoped ($T_c = 32$ K and $T_c = 25$ K) $Bi_{2-y}Pb_ySr_{2-z}La_zCuO_{6+\delta}$ [(Pb, La)-Bi2201] samples [11,12] exhibit checkerboard patterns (indicative of the simultaneous presence of both CDW domains) with $6.2 \pm 0.2a_0$, $5.1 \pm 0.2a_0$, and $4.5 \pm 0.2a_0$ unit cell ($a_0 = 3.83$ Å) periodicity, respectively. The increase in the CO wavelength with increased hole doping agrees well with x-ray scattering and STM measurements on Bi2201 without cation substitutions [4]. We have used the following formula from Ref. [43] to calculate the average number of holes per Cu for the (Pb, La)-Bi2201 samples in Ref. [11]: $T_c/T_c^{\max} = 1 - 250(p - 0.16)^2$,

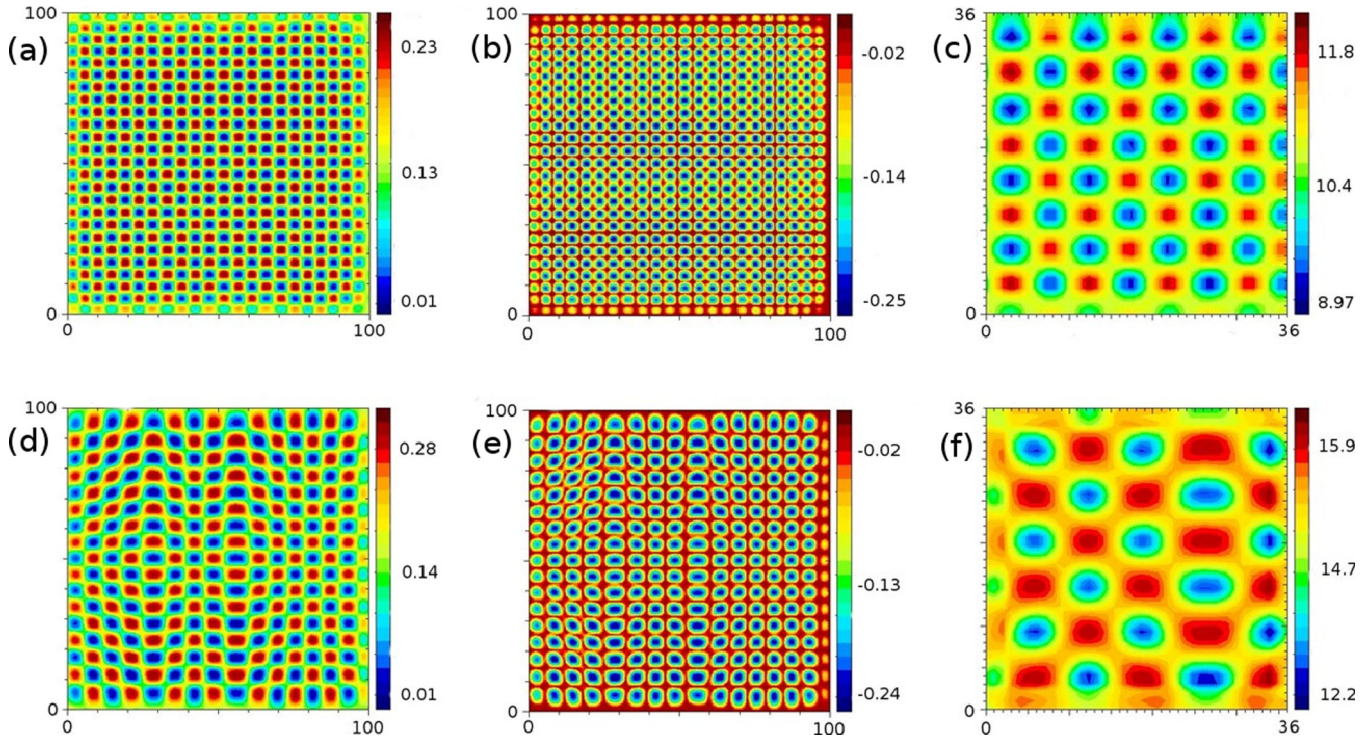

FIG. 2. Contour plots of the electronic density $p(\mathbf{r})$ calculated on a square lattice of 100 × 100 unit cells, assuming average charge densities of $p = 0.126$ in (a) and $p = 0.16$ in (d). The charge order wavelengths are $\lambda_{CO} = 4.5a_0$ in a and $\lambda_{CO} = 6.2a_0$ in (d), matching the checkerboard wavelength of the STM conductance maps of underdoped ($T_c = 25$ K; $p = 0.126$) and optimally doped (Pb, La)-Bi2201 in Ref. [11]. (b), (e), Corresponding spatial dependence of the free-energy potential $V_{GL}(\mathbf{r})$. (c), (f), Results of calculations of the d-wave pairing potential $\Delta_d(\mathbf{r})$ displayed over a 36 × 36 unit cell area (in meV unit). The spatial average value of the pair potential $\langle\Delta_d(\mathbf{r})\rangle$ is 9.2 meV at $p = 0.126$ in (c), and 15.8 meV at $p = 0.16$ in (f).

where $T_c^{\max} = 35$ K. This calculation yields $p = 0.126$ and $p = 0.141$ for the two underdoped samples. Figures 2(a) and 2(d) display CO checkerboard patterns simulated by the CH equation that resemble the STM differential conductance maps for (Pb, La)-Bi2201 at $p = 0.126$ and $p = 0.16$.

The CO periodicity is manifest in the spatial dependence of the free-energy potential $V_{GL}(\mathbf{r})$, shown in Figs. 1(b) and 1(e), and Figs. 2(b) and 2(e). The central assumption in our model is that by confining charge, a fluctuating CDW periodic potential that scales with $V_{GL}(\mathbf{r})$ mediates the attractive two-body SC interaction. In particular, we assume the fluctuating periodic potential has the same periodicity as the static CO detected experimentally and has a time-averaged potential well depth that is proportional to the depth of the static periodic potential. In what follows, we make the approximation that $\langle V_{GL}(\mathbf{r})\rangle$ is the pairing potential, where $\langle V_{GL}(\mathbf{r})\rangle$ is the spatial average of $V_{GL}(\mathbf{r})$ over a 100 × 100 unit cell area.

III. SUPERCONDUCTING CALCULATIONS IN THE CHARGE-ORDERED STATE

Next we use the free-energy simulations and experimentally determined input parameters for the optimally doped compounds to deduce the SC energy gap Δ_{SC}, the pseudogap Δ_{PG}, T_c, and T^* for the underdoped samples. To derive the local SC gap we solved the Bogoliubov-deGennes (BdG) equations via self-consistent calculations based on a Hubbard Hamiltonian [Eq. (B1)]. The calculations were performed for a sublattice about the center of the simulated charge density maps, using periodic boundary conditions and governed by self-consistent conditions for a spatially varying d-wave pairing potential $\Delta_d(\mathbf{r})$ and hole density $p(\mathbf{r})$ [Eqs. (B4) and (B5)]. We find that the spatial average $\langle\Delta_d(\mathbf{r})\rangle$ decreases with a reduction of p (below $p = 0.16$), but increases with decreasing λ_{CO}. The latter behavior is because as the two holes are forced closer together by the narrower confining potential the binding energy of the two-body interaction increases. The comparison between the charge simulations $p(\mathbf{r})$ [Figs. 1(a), 1(d), 2(a) and 2(d)] and the respective pairing potential $\Delta_d(\mathbf{r})$ [Figs. 1(c), 1(f), 2(c) and 2(f)] indicate that in our approach the pair amplitude has the same modulation as the charge order.

The values of $\langle V_{GL}(\mathbf{r})\rangle$ at optimal doping were multiplied by a scaling factor, such that the calculations [Figs. 1(f) and 2(f)] generate an average value of the pairing potential $\langle\Delta_d(\mathbf{r})\rangle$ for $p = 0.16$ that is close to the experimentally estimated value of the low-temperature SC gap Δ_{SC}. To calculate $\langle\Delta_d(\mathbf{r})\rangle$ for the underdoped samples (Tables I and II), this same scaling factor was subsequently applied to the respective values of $\langle V_{GL}(\mathbf{r})\rangle$. For (Pb, La)-Bi2201, the value of $\langle V_{GL}(\mathbf{r})\rangle$ varies little with doping, and hence p and λ_{CO} are responsible for the hole-doping dependence of $\langle\Delta_d(\mathbf{r})\rangle$. Experimental estimates of the SC gap for the $p = 0.126$ and 0.141 samples are not reported, but the calculated values of $\langle\Delta_d(\mathbf{r})\rangle$ for the underdoped samples (Table II) roughly follow the trend expected if the ratio $\Delta_{SC}/k_B T_c$ is independent of p. In contrast to (Pb, La)-Bi2201, the doping dependence of λ_{CO} in Y123 is weaker, and the CH

TABLE I. Experimental data for Δ_{SC} and Δ_{PG} determined from universal curves that describe Y123 and a number of other high-T_c cuprate superconductors [44]. An experimental value for Δ_{SC} at $p = 0.12$ is omitted, since deviations from the universal curve are expected for Y123 near 1/8 hole doping, where T_c plateaus. The value of $T^* \approx 278$ K at $p = 0.09$ is estimated from a linear extrapolation of data in Ref. [50]. We tune the scaling factors explained in the text to yield the blue and green values at optimum doping. Red values are calculated with the same parameters.

	$p = 0.16$	$p = 0.12$	$p = 0.09$
$\lambda_{CO}(a_0)$ [4,5,7]	3.49 ± 0.16	3.15 ± 0.16	3.00 ± 0.16
$\langle V_{GL}(\mathbf{r})\rangle$	-0.156	-0.110	-0.105
$\rho_b(1.05T_c)(\mu\Omega$ cm) [47]	≈ 40	≈ 50	≈ 70
Δ_{SC} [44] (meV)	42 ± 2	–	24 ± 1
$\langle \Delta_d(\mathbf{r})\rangle$ (meV)	43.8	25.5	23.3
T_c (K) [47,49]	93.4	66	55
	92.0	68.1	55.6
Δ_{PG} [44]	76	104	124
	76	93.4 ± 9	103.3 ± 9
T^* [49]	170	232	278
	170	209 ± 19	231 ± 21

simulations of charge stripes are characterized by a significant change in $\langle V_{GL}(\mathbf{r})\rangle$ with doping (Fig. 4). Consequently, the depth of the periodic potential plays an important role in the calculation of the doping dependence of $\langle \Delta_d(\mathbf{r})\rangle$ for Y123. The calculated values of $\langle \Delta_d(\mathbf{r})\rangle$ at $p = 0.09$ and 0.16 agree well with an empirical relation for $\Delta_{SC}(p)$ that describes a number of high-T_c cuprate superconductors [44]. The calculated result at $p = 0.12$ falls below this universal curve, which is consistent with the well-known plateau of $T_c(p)$ for Y123 near 1/8 hole doping.

TABLE II. Experimental data for Δ_{SC} and Δ_{PG} from STM with the indicated T_c values [11]. The hole doping p was determined from the T_c versus p relationship obtained by x-ray absorption experiments on (Pb, La)-Bi2201 and La-doped Bi2201 [43]. The in-plane resistivity ρ_{ab} data area for La-doped Bi2201 [46] and T^* data are from intrinsic tunneling measurements [48]. We tune the scaling factor explained in the text to yield the blue and green values at optimum doping. Red values are calculated without any extra parameters.

	$p = 0.16$	$p = 0.12$	$p = 0.09$
$\lambda_{CO}(a_0)$ [11]	6.2 ± 0.2	5.1 ± 0.2	4.5 ± 0.2
$\langle V_{GL}(\mathbf{r})\rangle$	-0.1022	-0.1018	-0.1021
$\rho_b(1.05T_c)(\mu\Omega$ cm) [46]	18.3	24.8	28.3
Δ_{SC} [11] (meV)	15	–	–
$\langle \Delta_d(\mathbf{r})\rangle$ (meV)	15.8	13.2	9.2
T_c (K) [11]	35	32	25
	35.2	32.5	24.7
Δ_{PG} [12]	30 ± 12	45 ± 15	68 ± 20
	30	44.3	54.2
T^* [48]	241	355	446
	241	327.9	427.4

An estimate of T_c is obtained by self-consistently solving the BdG equations with a temperature-dependent GL potential

$$V(T,p) = V(0,p)[1 - T/T_{PS}(p)]^2, \quad (2)$$

where we take $V(0,p) \approx \langle V_{GL}(\mathbf{r},p)\rangle$ and the temperature $T_{PS}(p)$ below which phase separation occurs to be equal to $T^*(p)$ in the calculations. Because of the BdG approach and the above equation, the value of $\langle \Delta_d(\mathbf{r},T)\rangle$ decreases with increasing temperature, but it remains finite in many regions of the system for a significant range of temperature above T_c. This is consistent with the body of experimental results on cuprates mentioned earlier that are suggestive of persisting SC correlations above T_c [34–40]. Typical $\langle \Delta_d(\mathbf{r},T)\rangle \equiv \langle \Delta_d(p,T)\rangle$ plots of three different Y123 compounds are shown in Fig. 8.

Next we assume that bulk superconductivity is achieved via Josephson coupling between different closely spaced patches of intertwined CO and SC pairing. We assume there is SC phase coherence within the patches, and that there are many such closely spaced SC domains slightly above $T_c(p)$ forming junctions with an average tunnel resistance that is proportional to the normal-state resistance immediately above $T_c(p)$. As explained previously [45], for a d-wave superconductor in single-crystal form it is sufficient to use the following relation for the average Josephson coupling energy:

$$\langle E_J(p,T)\rangle = \frac{\pi\hbar\langle \Delta_d(\mathbf{r},T)\rangle}{2e^2 R_n(p)} \tanh\left[\frac{\langle \Delta_d(\mathbf{r},T)\rangle}{2k_B T}\right], \quad (3)$$

where $\langle \Delta_d(\mathbf{r},T)\rangle = \sum_i^N \langle \Delta_d(r_i,p,T)\rangle/N$ is the pairing potential. The quantity $R_n(p)$ is proportional to the normal state in-plane resistivity $\rho_{ab}(p, T \geqslant T_c)$. In what follows we assume $R_n(p)$ for the optimally doped compounds, and in the case of (Pb, La)-Bi2201 use experimental values of the in-plane resistivity ratio $\rho_{ab}(p)/\rho_{ab}(p = 0.16)$ to calculate $R_n(p)$ for the underdoped samples. Since the relationship between T_c/T_c^{max} and the hole concentration p for (Pb, La)-Bi2201 is the same as for La-doped Bi2201 [43], we have used available resistivity data for La-doped Bi2201 [46] in our calculations shown in Table II. For orthorhombic Y123, we instead used experimental values of the b-axis resistivity ratio $\rho_b(p)/\rho_b(p = 0.16)$ from Ref. [47] to estimate $R_n(p)/R_n(p = 0.16)$.

As the temperature is lowered below T^*, thermal fluctuations diminish and long-range phase coherence between the individual SC domains is established when $k_B T \approx \langle E_J(p,T)\rangle$. The temperature T at which this occurs defines the bulk critical temperature T_c. Figures 3(a) and 3(b) show the temperature dependence of $\langle E_J(p,T)\rangle$ for both compounds at the different dopings. The intersection of the $\langle E_J(p,T)\rangle$ curves with the $k_B T$ line yields values of T_c in good agreement with the actual values for Y123 and (Pb, La)-Bi2201 (Fig. 4 and Tables I and II).

IV. PSEUDOGAP

Next, we use the free-energy simulations to make a simple estimate of the PG, under the assumption that the PG appears due to mesoscale phase separation [27] that creates small domains of CO wavelength below $T_{PS} \approx T^*$. For Bi2201 we consider a single-particle state bound to a two-dimensional (2D) square box of depth $\langle V_{GL}(\mathbf{r})\rangle$ and sides of length λ_{CO}.

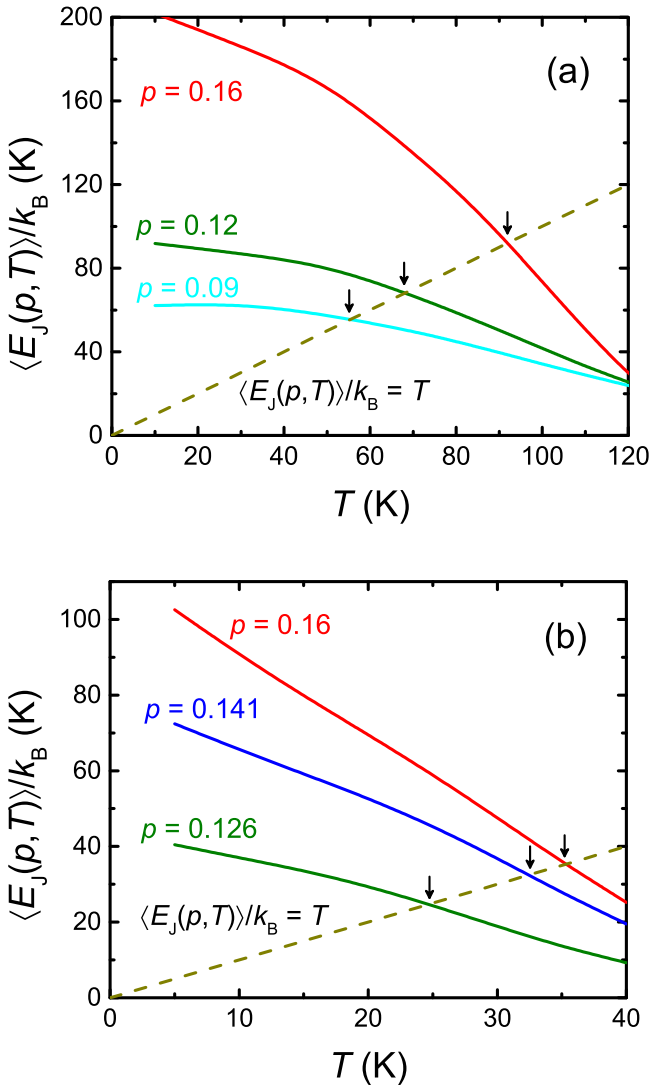

FIG. 3. Calculated values of the superconducting transition temperature. (a), (b) The temperature dependence of the average Josephson coupling energy $\langle E_J(p,T)\rangle$ (divided by Boltzmann constant k_B) for Y123 at $p = 0.09$,0.12, and 0.16 in (a), and (Pb, La)-Bi2201 at $p = 0.126$,0.141, and 0.16 in (b). The values of T_c correspond to the intersections of the dashed straight line $\langle E_J(p,T)\rangle/k_B = T$ with the $\langle E_J(p,T)\rangle/k_B$ curves and are marked by the arrows.

For Y123 we consider a single-particle state bound to a stripelike 2D rectangular box of depth $\langle V_{GL}(\mathbf{r})\rangle$, width λ_{CO}, and length equivalent to the CDW correlation length, which is much longer than λ_{CO} [4,5,7]. We assume in both cases that the PG is proportional to the numerical solution of the corresponding 2D Schrödinger equation for the ground-state binding energy. The proportionality factor is estimated using experimental values of the pseudogap Δ_{PG} for Y123 and (Pb, La)-Bi2201 at $p = 0.16$ (Tables I and II), and the values of Δ_{PG} are calculated for the underdoped samples using the respective values of $\langle V_{GL}(\mathbf{r})\rangle$ and λ_{CO}. To further assess the accuracy of the results for the underdoped samples, we convert Δ_{PG} to T^* using the experimental ratios $T^*/\Delta_{PG} = 170$ K/76 meV and $T^*/\Delta_{PG} = 241$ K/ 30 meV for optimally doped Y123 and (Pb, La)-Bi2201, respectively. As shown in Fig. 4 and Table II, the calculated values of T^* for (Pb, La)-Bi2201 at $p = 0.126$ and 0.141 agree well with measurements of the PG onset temperature for La-doped Bi2201 [48]. Reasonable agreement is also obtained between the calculated and experimental [49] values of T^* for Y123 at $p = 0.09$ and 0.12 (Fig. 4 and Table I). As mentioned in the introduction we presume the onset of CO domains at $T^* > T_{CO}(p)$, as suggested by some experiments [3,7,9,28].

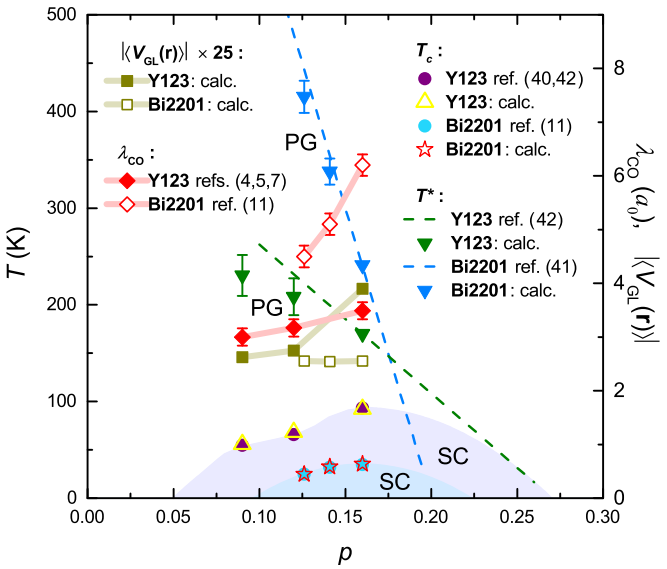

FIG. 4. Comparison of experimental and calculated values of T_c and T^* versus hole doping. Also shown is the experimentally determined doping dependence of the charge order wavelength λ_{CO} for both compounds, as well as the doping dependence of the calculated absolute value of the spatial average of the free-energy potential $|\langle V_{GL}(\mathbf{r})\rangle|$. For display purposes $|\langle V_{GL}(\mathbf{r})\rangle|$ is shown multiplied by a factor of 25.

V. COMPARISON OF CALCULATED AND EXPERIMENTAL PARAMETERS

Tables I and II contain values of experimental parameters (denoted by black text) used in the calculations for each compound, and the calculated parameters (denoted by red text). For each cuprate family the calculated values at $p = 0.16$ (which are denoted by blue and green text) were multiplied by a scaling factor to match experimental values as follows:

(i) The proportionality constant between $\langle V_{GL}(\mathbf{r})\rangle$ and the attractive pairing potential V of Eq. (B4) was adjusted to yield a calculated value of $\langle \Delta_d(\mathbf{r})\rangle$, which approximately equals the experimental value of the SC gap Δ_{SC} at $p = 0.16$. This proportionality constant, once determined, was subsequently used for all other values of p.

(ii) The scaling factor between the normal resistance R_n in Eq. (3) and the resistivity $\rho_b(1.05Tc)$ just above T_c was adjusted until the calculated value of T_c at $p = 0.16$ approximately equaled the experimental value. This same scaling factor was used for all other values of p.

(iii) The ground-state binding energy of a single particle in a 2D square (rectangular) box was multiplied by a proportionality factor so as to equal the PG of (Pb, La)-Bi2201 (Y123) at $p = 0.16$. Again, this same proportionality constant was used for the calculations at other dopings.

VI. FERMI-ARC FORMATION

Next we show that the phase separation approach considered above is able to reproduce the ungapped portion of the Fermi surface (Fermi arcs) that is known to occur near the nodal region just above T_c [51–53]. We start by recalling that Figs. 1(c), 1(f), 2(c), and 2(f) show domains of SC order parameter modulations. To each domain we assign a label j and a complex SC order parameter $\Delta_d(k,T)\exp(i\Phi_j)$, where $\Delta_d(k,T) = \Delta_0(T)[\cos(k_x a_0) - \cos(k_y a_0)] = \Delta_0(T)\cos(2\phi)$, ϕ is the azimuthal angle measured from the x direction in the CuO_2 plane and $\Delta_0(T)$ is the wave function amplitude in the jth domain at temperature T. The d-wave symmetry implies larger supercurrents flowing in the CuO_2 plane along the antinodal directions parallel to the Cu-O bonds, and vanishing values along the nodal directions $\phi = \pm\pi/4$ and $\pm\pi/4$. The local intrinsic SC phase Φ_j and the superfluid density $n_j \propto \Delta_d(r_j,T)^2$ are canonically conjugate variables [54], leading to large fluctuations of the phase Φ_j along the nodal directions, where n_j and Δn_j vanish. This is due to the quantum uncertainty principle and we may write $\Delta\Phi_j(\phi) \propto 1/\cos(2\phi)$ to indicate the azimuthal dependence of the phase uncertainty, which has its maximum and minimum values along the nodal and antinodal directions, respectively. Furthermore, $\Delta\Phi_j$ has a clear dependence on the Josephson coupling. In particular, as shown in the previous section, at $T < T_c$ all Φ_j are locked together leading to long-range SC order, but at $T > T_c$ phase decoupling occurs because $\langle E_J(p,T)\rangle < k_B T$ and concomitantly $\Delta\Phi_j$ increases with T up to the temperature at which $\langle E_J(p,T)\rangle$ vanishes. In particular, $\Delta\Phi_j$ increases monotonically from near zero at T_c to very large values near T^*. Furthermore, $\Delta\Phi_j$ has a large anisotropy when combined with the quantum effects discussed above. The two distinct contributions are separable, such that $\Delta\Phi_j(p,T,\phi) = \Delta\Phi_j(p,T)\Delta\Phi_j(\phi)$. We drop the index j because $\Delta\Phi_j(\phi)$ is the same for all domains, and assume $\langle E_J(p,T)\rangle$ is the same for all j. These considerations imply that just above T_c the electrons ejected by angle-resolved photoemission spectroscopy (ARPES) from different domains come from regions where the SC order parameter has essentially the same Φ_j along the antinodal directions, and $\Delta\Phi_j(\phi) \approx 0$. On the other hand, such phase coherence is lost near the nodal directions where $\Delta\Phi_j(\phi) \approx \pi$ is maximum. Consequently, the average SC amplitude measured by ARPES may be written as follows [55]

$$\begin{aligned}\langle\Delta_d(p,T,\phi)\rangle &= \frac{|\cos(2\phi)|}{\Delta\Phi_j(p,T,\phi)}\int_0^{\Delta\Phi_j(p,T,\phi)}\langle\Delta(p,T)\rangle\cos(\Phi)d\Phi \\ &= \langle\Delta(p,T)\rangle|\cos(2\phi)|\frac{1}{\Delta\Phi_j(p,T,\phi)}\sin[\Delta\Phi_j(p,T,\phi)].\end{aligned} \tag{4}$$

This expression contains the two distinct contributions that weaken phase coherence—one from quantum oscillations that depends only on the azimuthal angle ϕ and one from thermal oscillations that competes with the average Josephson coupling, leading to $\Delta\Phi_j(p,T,\phi) = \Delta\Phi_j(p,T)\Delta\Phi_j(\phi)$ for all j. We take $\Delta\Phi(\phi) \sim 1/\cos^2(2\phi)$, which satisfies the expected inverse cosine dependence and the square makes it symmetric and always positive around the nodal directions ($\phi = \pm\pi/4$ and $\pm\pi/4$). We infer the functional form of $\Delta\Phi(p,T)$ noting that for $T < T_c$, all Φ_j are locked together leading to long-range order and $\Delta\Phi_j \sim 0$. On the other hand, for $T \leqslant T_c$ all Φ decouple because $\langle E_J(p,T)\rangle < k_B T$ and $\Delta\Phi > 0$. Above T_c, $\langle E_J(p,T)\rangle$ decreases with increasing T and vanishes near T^*. Concomitantly $\Delta\Phi$ increases. Thus, there are three distinct temperature-dependent regimes:

(i) $T \leqslant T_c$: Since $\Delta\Phi \sim 0$, Eq. (4) is easy to solve and we obtain the bare expression $\langle\Delta_d(\mathbf{r},T,\phi)\rangle = \langle\Delta_d(p,T)\rangle|\cos(2\phi)|$.

(ii) $T > T^*$: $\langle\Delta(p,T)\rangle \sim 0$ and it is clear that there is no gap.

(iii) $T_c < T$: Taking into account the effect of $\langle E_J(p,T)\rangle$ we assume $\Delta\Phi(p,T) = A[1 - \langle E_J(p,T)\rangle/k_B T_c(p)$ where A is a constant. This expression vanishes at T_c and increases monotonically with p, as expected from ARPES experiments [51,52]. Thus, accounting for the quantum ($\sim 1/\cos^2(2\phi)$) and the thermal contributions ($T > T_c$), $\Delta\Phi(p,T,\phi) = [A/\cos^2(2\phi)][1 - \langle E_J(p,T)\rangle/k_B T_c(p)$ and we obtain the value of A by comparing with the onset of the measured [51] gapless region for a given sample. To reproduce the measured gapless regions we also assume in Eq. (4) that $\langle\Delta_d(p,T,\phi)\rangle \sim 0$ whenever $\Delta\Phi(p,T,\phi) \geqslant \pi$, due to destructive phase interference from electrons ejected from different domains.

To obtain the constant A we use the ARPES measurements [51] at $T = 102$ K for the Bi2212 compound with $T_c = 92$ K, which shows a gapless region between $28^\circ \leqslant \phi \leqslant 62^\circ$. Equating $\Delta\Phi(p \sim 0.15, T = 102\text{K}, \phi = 28^\circ, 62^\circ) = \pi$, yields $\langle\Delta_d(p,T,\phi)\rangle \sim 0$ and this is possible if we take $A = 2.84\pi$. Note that ϕ is measured from the (π,π) to $(0,\pi)$ direction of the Brillouin zone according to Refs. [51] and [52]. With $\Delta\Phi(p,T,\phi)$ determined, we may apply the derived equation to any sample. In particular, we apply this expression to the other two Bi2212 compounds measured in Ref. [51].

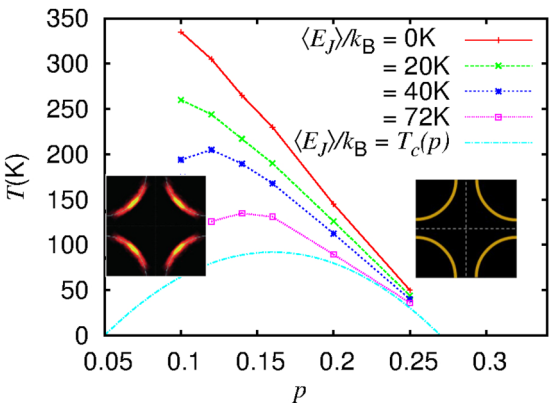

FIG. 5. Josephson coupling energy phase diagram and schematic Fermi surface. The variation of the average Josephson coupling energy with doping and temperature for Bi2212 (from Ref. [45]). Above the onset of $\langle E_J\rangle/k_B = 0$ K there is no SC gap. The corresponding gapless Fermi surface is depicted at the right of the phase diagram. In the region of the phase diagram where $T \geqslant T_c$, the average SC gap may be finite. However, combined thermal and quantum phase fluctuations may cause destructive interference in the ARPES data along the nodal directions, leading to the gapless Fermi arcs shown in the left of the figure.

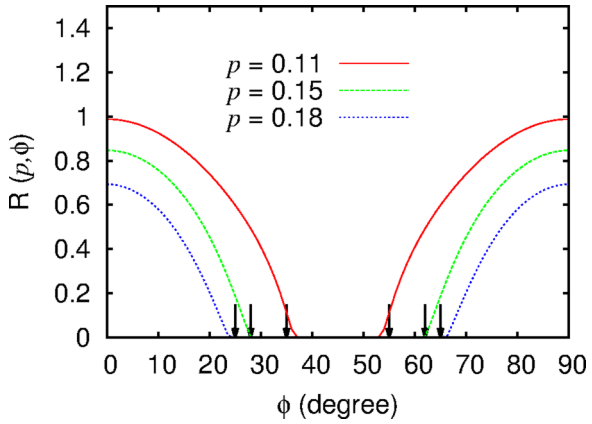

FIG. 6. The envelope of the SC amplitude $\langle \Delta_d(p,T,\phi)\rangle$ according to Eq. (4). The arrows show the limits of the gapless region as determined from ARPES experiments on Bi2212 at $T = T_c(p) + 10$ K for three dopings [51].

Some values of $\langle E_J(p,T)\rangle$ above T_c used in the calculations are plotted in Fig. 5. Accordingly, we obtain for the $T_c = 86$ K compound a gapless region at $23.8^\circ \leqslant \phi \leqslant 66.2^\circ$, which compares well with the experimental gapless range $25^\circ \leqslant \phi \leqslant 65^\circ$. For the underdoped $T_c = 75$ K Bi2212 sample at $T = 85$ K, we obtain $36.5^\circ \leqslant \phi \leqslant 53.5^\circ$, which is also in good agreement with the experimental result [51]. We summarize the Fermi-arc calculations for the three samples in Fig. 6, where the results of the envelope phase factor of $\langle \Delta_d(p,T,\phi)\rangle$

$$R = \frac{|\cos(2\phi)|}{\Delta\Phi(p,T,\phi)} \times \sin[\Delta\Phi_j(p,T,\phi)] \qquad (5)$$

from Eq. (4) are in good agreement with the experiments [51]. The arrows mark the experimentally determined onset of the gapless regions for each sample, as described above.

VII. SUMMARY AND CONCLUSIONS

Our theory infers a fundamental link between the periodicity of the CDW order and the PG and SC energy scales of high-temperature cuprate superconductors, and shows that within this framework it is possible to account for the onset temperatures T_c and T^* of two different cuprate families. We stress that the only quantitative assumptions made in our calculations for underdoped Y123 and (Pb, La)-Bi2201 pertain to unknown proportionality constants, which we have determined by scaling calculated free-energy parameters to achieve values of the PG and SC gap that agree with experimental values at one particular doping. Our model is general in the sense that it can be applied to other cuprate families, provided the doping dependence of the CDW order is known.

Our approach generates a local free-energy potential having a spatial periodicity that matches that of the experimentally observed short-range static CDW order. Our calculations in the framework of BdG theory yield different SC amplitudes in distinct charge-ordered domains that generally vanish only above T_c. Our approach is consistent with experiments [9,11,36,38] that measure a finite SC amplitude above T_c, and promotes the scenario whereby the SC resistive transition marks the onset of global phase coherence between SC domains. In our model Fermi arcs appear above T_c because there are large phase fluctuations along the nodal directions where the superfluid density vanishes. The increase of the arcs' size with p is reproduced because the dependence of $\langle E_J(p,T)\rangle$ on the temperature changes rapidly with doping.

Finally, we address the experimental observations indicating a competition between superconductivity and CO. While x-ray experiments show a decrease of the CDW diffraction intensity and correlation length below T_c [1,2,4,5,8], these measurements seem to be detecting static charge correlations. Static CDW order competes with superconductivity by reducing the number of charge carriers available for pairing. On the other hand, our theory requires that dynamic CO is also present to induce a fluctuating hole-pair potential that scales with V_{GL}. While there is some evidence for CDW fluctuations from optical pump-probe [56] and low-energy, momentum-resolved electron energy-loss spectroscopy [50] experiments, there is currently insufficient experimental information to assess the pervasiveness or significance of fluctuating CO in cuprates.

ACKNOWLEDGMENTS

We thank S. Ono and Y. Ando for providing us with their resistivity data. We also thank Andrea Damascelli, André-Marie Tremblay, and John Tranquada for informative discussions. Supported by the Brazilian agencies FAPERJ and CNPq (E.V.L.M.), the Canadian Institute for Advanced Research (CIFAR), and the Natural Sciences and Engineering Research Council of Canada (J.E.S.).

APPENDIX A: CHARGE ORDER SIMULATIONS

To describe the growth and development of spatial charge inhomogeneity in the CuO_2 planes we applied a theory of phase-ordering dynamics, whereby the system evolves through domain coarsening when quenched from a homogeneous into a broken-symmetry phase. The time-dependent CH approach provides a simple way to determine the time evolution of the CO process [41]. The CH equation can be written in the form of the following continuity equation for the local free-energy current density $\mathbf{J} = -M\nabla^2((\partial f/\partial u)$ [57]

$$\frac{\partial u}{\partial t} = -\nabla.\mathbf{J} = -M\nabla^2\left[\varepsilon^2\nabla^2 u + \frac{\partial V_{GL}}{\partial u}\right], \qquad (A1)$$

where M is the charge mobility that sets the phase separation time scale. The order parameter varies between $u(\mathbf{r},t) \sim 0$ for the homogeneous system above the phase separation onset temperature T_{PS}, and $u(\mathbf{r},t \to \infty) = \pm 1$ for the extreme case of complete phase separation. We solved the CH equation by a stable and fast finite difference scheme with free boundary conditions [55]. The spatial dependence of the charge density obtained by numerically solving the CH equation evolves with time $t = n\delta t$, where n is the number of time steps δt. When the order parameter is conserved, as in phase separation, the charges can only exchange locally rather than over large distances. This leads to diffusive transport of the order parameter. Consequently, at early times or small n, we obtain charge modulations with periodicities of only a few lattice constants. Using different parameters and initial conditions

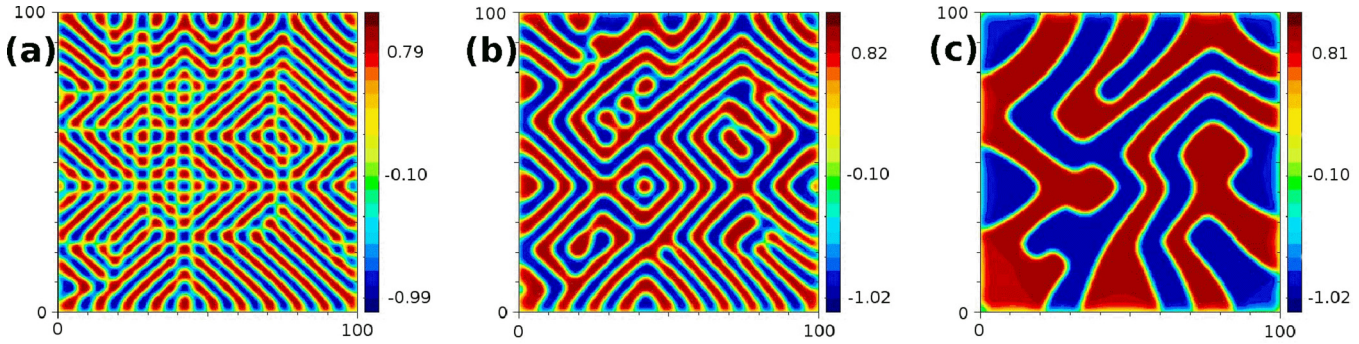

FIG. 7. Two-dimensional CH simulations of $u(r,t)$ for $\alpha = B = 1$, $\varepsilon = 0.012$ and time steps (a) $n = 900$, (b) $n = 1500$, and (c) $n = 9000$. These plots are continuation of the time evolution of Fig. 2(a) with $n = 700$.

we are able to reproduce the experimentally determined CO patterns in cuprates. Although these simulations are not the stable solutions of the CH equation (as is clear from the time evolution of the simulations shown in Fig. 7), the aim here is to generate periodic charge modulations with experimentally determined wavelengths that can be subsequently used to calculate the SC gap and PG in our phase separation model. For convergence the time step δt and spatial step $h \approx 1/N$ for a square lattice of N^2 sites must be such that $\delta t \leqslant h^2/9$ [55]. For the calculations here we used $\delta t \leqslant h^2/10$ and $h = 1/100$.

In the main paper we present detailed CO, T_c and T^* calculations for six compounds. Three of the Bi2201 and three of the Y123 families. In the following, we give the values of some parameters used in the CH simulations.

(Pb, La)-Bi2201: Simulations with $\alpha = B = 1$, time steps of $n = 700,900,1300$ and $\varepsilon = 0.012,0.014,0.0175$ yield checkerboard CO patterns with the desired wavelengths λ_{CO} for (Pb, La)-Bi2201 (at $p = 0.126,0.141$ and 0.16) near $4.5a_0$, $5.1a_0$, and $6.2a_0$, respectively. The fewer time steps required to simulate the CO patterns of the underdoped samples is indicative of a reduced charge mobility, and is consistent with an increase of the normal-state resistivity. At later times (i.e., greater n) the periodic electronic structure evolves into an irregular patchlike system of segregated low- and high-charge density regions. In addition, the length scale of the system increases with the phase separated regions forming larger domains. This latter situation was considered previously [45]. Figure 7 shows CH simulations of $u(\mathbf{r},t)$ at times beyond where checkerboard CO with $\lambda_{CO} = 4.5a_0$ is observed in (Pb, La)-Bi2201 at $p = 0.126$.

Y123: Simulations with $\alpha = 1$, $B = 5$, $\varepsilon = 0.0053$, 0.0055, 0.0058, and time steps $n = 35,38,42$ yield charge stripe patterns with the desired wave vectors $Q = 0.333,0.317$, and 0.287 reciprocal-lattice units ($\lambda_{CO} = 1/Q$) estimated from Refs. [4,5,7] for Y123 at $p = 0.09,0.12$ and 0.16, respectively. Note that the values of n are much shorter than needed to simulate the checkerboard CO patterns of (Pb, La)-Bi2201. Because of the fewer time steps, the simulations for Y123 are somewhat less sharp.

APPENDIX B: COMBINED BOGOLIUBOV-DEGENNES (BDG) AND CAHN-HILLIARD (CH) CALCULATIONS

We performed self-consistent calculations with the BdG theory [58,59] for each of the CH simulated charge density maps [Figs. 1(a) and 1(d), and Figs. 2(a) and 2(d)]. To calculate the SC pairing amplitude we assumed the attractive interaction potential V scales with $\langle V_{GL}(\mathbf{r})\rangle$. The SC calculations begin with the extended Hubbard Hamiltonian [58,59]. To describe the charge carrier's dynamics in the CuO_2 planes of the HTSC we consider this Hamiltonian in a square lattice

$$H = -\sum_{\{ij\}\sigma} t_{ij} c^{\dagger}_{i\sigma} c_{j\sigma} + \sum_{i\sigma} \mu_i n_{i\sigma} + U \sum_i n_{i\uparrow} n_{i\downarrow} - \frac{V}{2} \sum_{\langle ij\rangle\sigma\sigma'} n_{i\sigma} n_{j\sigma'}, \tag{B1}$$

where $c^{\dagger}_{i\sigma}(c_{i\sigma})$ is the usual fermionic creation (annihilation) operator at site i, the spin σ is up $\uparrow$ or down $\downarrow$. $n_{i\sigma} = c^{\dagger}_{i\sigma} c_{i\sigma}$ is the number operator, and t_{ij} is the hopping between sites i and j. U is the magnitude of the on-site repulsion, and V is the magnitude of the nearest-neighbor attractive interaction. μ_i is the local chemical potential derived in the self-consistent process through which the local charge density is calculated by the CH equation and is maintained fixed. For (Pb, La)-Bi2201 we used nearest-neighbor hopping $t = 0.15$eV, next-nearest-neighbor hopping $t_2 = -0.27t$, and third nearest-neighbor hopping $t_3 = 0.19t$ derived from ARPES dispersion relations [60]. For Y123, we used the ARPES results $t = 0.15$meV, $t_2 = -0.50t$, and $t_3 = 0.16t$ [61]. The BdG mean-field equations are [59]

$$\begin{pmatrix} K & \Delta_d(\mathbf{r}) \\ \Delta^*_d(\mathbf{r}) & -K^* \end{pmatrix} \begin{pmatrix} u_n(\mathbf{r}) \\ v_n(\mathbf{r}) \end{pmatrix} = E_n \begin{pmatrix} u_n(\mathbf{r}) \\ v_n(\mathbf{r}) \end{pmatrix} \tag{B2}$$

with

$$K u_n(\mathbf{r}) = -\sum_{\mathbf{R}} t_{\mathbf{r},\mathbf{r}+\mathbf{R}} u_n(\mathbf{r}+\mathbf{R}) + \mu(\mathbf{r}) u_n(\mathbf{r})$$

$$\Delta_d u_n(\mathbf{r}) = \sum_{\mathbf{R}} \Delta_d(\mathbf{r}) u_n(\mathbf{r}+\mathbf{R}), \tag{B3}$$

and similar equations for $v_n(\mathbf{r})$, where $\mathbf{r}+\mathbf{R}$ is the position of the nearest-neighbor sites, and $\mu(\mathbf{r}) \equiv \mu_i$ is the local chemical potential. These equations are solved numerically for eigenvalues $E_n(\geqslant 0)$ self-consistently with the spatially

varying d-wave pairing potential [58]

$$\Delta_d(\mathbf{r}) = -\frac{V}{2}\sum_n [u_n(\mathbf{r})v_n^*(\mathbf{r}+\mathbf{R}) + v_n^*(\mathbf{r})u_n(\mathbf{r}+\mathbf{R})]\tanh\frac{E_n}{2k_BT}, \quad \text{(B4)}$$

where $V = V(T,p)$ was defined in Eq. (2). The results of $\langle\Delta_d(\mathbf{r},T)\rangle$ are plotted in Fig. 8 for the three compounds of the Y123 system. Concomitantly, the spatially varying hole density of charge carriers is given by

$$p(\mathbf{r}) = 1 - 2\sum_n [|u_n(\mathbf{r})|^2 f_n + |v_n(\mathbf{r})|^2(1-f_n)], \quad \text{(B5)}$$

where $f_n = [\exp(E_n/k_BT+1]^{-1}$ is the Fermi occupation function. It is important to emphasize that the spatially inhomogeneous distribution of charge generated by the CH equation for different dopings was kept fixed while the local chemical potential $\mu(\mathbf{r})$ was self-consistently determined in the convergence process. This procedure incorporates the charge inhomogeneity in the calculations in a natural way.

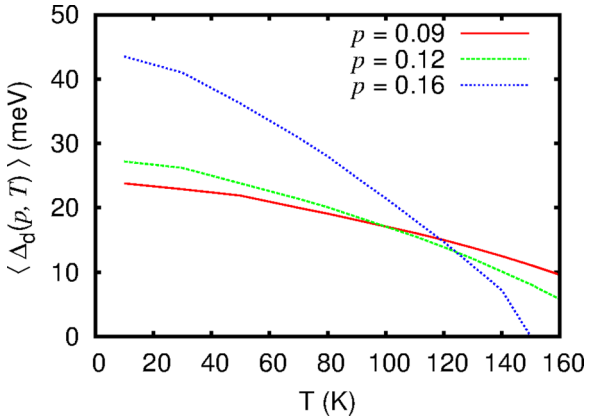

FIG. 8. Example of calculated $\langle\Delta_d(p,T)\rangle$ used to obtain T_c: The average SC amplitudes for Y123 from BdG Eq. (B4) used in the calculations of $\langle E_J(p,T)\rangle$ [see Eq. (3)]. The low-temperature limits of $\langle\Delta_d(p,T=0)\rangle$ are also listed in Table I.

[1] J. Chang, E. Blackburn, T. Holmes, N. B. Christensen, J. Larsen, J. Mesot, R. Liang, D. A. Bonn, W. N. Hardy, A. Watenphul, M. V. Zimmermann, E. M. Forgan, and S. M. Hayden, Direct observation of competition between superconductivity and charge density wave order in $YBa_2Cu_3O_{6.67}$, Nature Phys. **8**, 871 (2012).

[2] G. Ghiringhelli, M. Le Tacon, M. Minola, S. Blanco-Canosa, C. Mazzoli, N. B. Brookes, G. M. D. Luca, A. Frano, D. G. Hawthorn, F. He, T. Loew, M. Moretti Sala, D. C. Peets, M. Salluzzo, E. Schierle, R. Sutarto, G. A. Sawatzky, E. Weschke, B. Keimer, and L. Braicovich, Long-range incommensurate charge fluctuations in $(Y,Nd)Ba_2Cu_3O_{6+x}$, Science **337**, 821 (2012).

[3] R. Comin, A. Frano, M. M. Yee, Y. Yoshida, H. Eisaki, E. Schierle, E. Weschke, R. Sutarto, F. He, A. Soumyanarayanan, Y. He, M. L. Tacon, I. S. Elfimov, J. E. Hoffman, G. A. Sawatzky, B. Keimer, and A. Damascelli, Charge order driven by Fermi-arc instability in $Bi_2Sr_{2-x}La_xCuO_{6+\delta}$, Science **343**, 390 (2014).

[4] S. B.-Canosa, A. Frano, E. Schierle, J. Porras, T. Loew, M. Minola, M. Bluschke, E. Weschke, B. Keimer, and M. Le Tacon, Resonant x-ray scattering study of charge-density wave correlations in $YBa_2Cu_3O_{6+x}$, Phys. Rev. B **90**, 054513 (2014).

[5] M. Hücker, N. B. Christensen, A. T. Holmes, E. Blackburn, E. M. Forgan, R. Liang, D. A. Bonn, W. N. Hardy, O. Gutowski, M. V. Zimmermann, S. M. Hayden, and J. Chang, Competing charge, spin, and superconducting orders in underdoped $YBa_2Cu_3O_y$, Phys. Rev. B **90**, 054514 (2014).

[6] E. H. D. S. Neto, R. Comin, F. He, R. Sutarto, Y. Jiang, R. L. Greene, G. A. Sawatzky, and A. Damascelli, Charge ordering in the electron-doped superconductor $Nd_{2-x}Ce_xCuO_4$, Science **347**, 282 (2015).

[7] R. Comin, R. Sutarto, E. H. D. S. Neto, L. Chauviere, R. Liang, W. N. Hardy, D. A. Bonn, F. He, G. A. Sawatzky, and A. Damascelli, Broken translational and rotational symmetry via charge stripe order in underdoped $YBa_2Cu_3O_{6+y}$, Science **347**, 1335 (2015).

[8] R. Comin, R. Sutarto, F. He, E. H. D. S. Neto, L. Chauviere, A. Fraño, R. Liang, W. N. Hardy, D. A. Bonn, Y. Yoshida, H. Eisaki, A. J. Achkar, D. G. Hawthorn, B. Keimer, G. A. Sawatzky, and A. Damascelli, Symmetry of charge order in cuprates, Nature Mater. **14**, 796 (2015).

[9] E. H. D. S. Neto, P. Aynajian, A. Frano, R. Comin, E. Schierle, E. Weschke, A. Gyenis, J. Wen, J. Schneeloch, Z. Xu, S. Ono, G. Gu, M. L. Tacon, and A. Yazdani, Ubiquitous interplay between charge ordering and high-temperature superconductivity in cuprates, Science **343**, 393 (2014).

[10] K. Fujita, M. H. Hamidian, S. D. Edkins, C. K. Kim, Y. Kohsaka, M. Azuma, M. Takano, H. Takagi, H. Eisaki, S.-i. Uchida, A. Allais, M. J. Lawler, E.-a. Kim, S. Sachdev, and J. C. S. Davis, Direct phase-sensitive identification of a d-form factor density wave in underdoped cuprates, Proc. Nat. Acad. Sci. **111**, E3026 (2014).

[11] W. D. Wise, M. C. Boyer, K. Chatterjee, T. Kondo, T. Takeuchi, H. Ikuta, Y. Wang, and E. W. Hudson, Charge density wave origin of cuprate checkerboard visualized by scanning tunneling microscopy, Nature Phys. **4**, 696 (2008).

[12] W. D. Wise, Kamalesh Chatterjee, M. C. Boyer, T. Kondo, T. Takeuchi, H. Ikuta, Z. Xu, J. Wen, G. D. Gu, Y. Wang, and E. W. Hudson, Imaging nanoscale Fermi-surface variations in an inhomogeneous superconductor, Nature Phys. **5**, 213 (2009).

[13] J. E. Hoffman, E. W. Hudson, K. M. Lang, V. Madhavan, H. Eisaki, S. Uchida, and J. C. Davis, A four-unit-cell periodic pattern of quasiparticle states surrounding vortex cores in $Bi_2Sr_2CaCu_2O_{8+d}$, Science **295**, 466 (2002).

[14] C. Howald, H. Eisaki, N. Kaneko, M. Greven, and A. Kapitulnik, Periodic density-of-states modulations in superconducting $Bi_2Sr_2CaCu_2O_{8+\delta}$, Phys. Rev. B **67**, 014533 (2003).

[15] M. Vershinin, S. Misra, S. Ono, Y. Abe, Y. Ando, and A. Yazdani, Local ordering in the pseudogap state of the high-T c superconductor $Bi_2Sr_2CaCu_2O_{8+\delta}$, Science **303**, 1995 (2004).

[16] T. Hanaguri, C. Lupien, Y. Kohsaka, D-H Lee, M. Azuma, M. Takano, H. Takagi, and J. C. Davis, A 'checkerboard' electronic crystal state in lightly hole-doped $Ca_{2-x}Na_xCuO_2Cl_2$, Nature (London) **430**, 1001 (2004).

[17] K. McElroy, D.-H. Lee, J. Hoffman, K. Lang, J. Lee, E. Hudson, H. Eisaki, S. Uchida, and J. C. Davis, Coincidence of Checkerboard Charge Order and Antinodal State Decoherence in Strongly Underdoped Superconducting $Bi_2Sr_2CaCu_2O_{8+\delta}$, Phys. Rev. Lett. **94**, 197005 (2005).

[18] W. Tabis, B. Yu, I. Bialo, M. Bluschke, T. Kolodziej, A. Kozlowski, Y. Tang, E. Weschke, B. Vignolle, M. Hepting, H. Gretarsson, R. Sutarto, F. He, M. Le Tacon, N. Barišić, G. Yu, and M. Greven, New insight into cuprate charge order from X-ray measurements of $HgBa_2CuO_{4+\delta}$, arXiv:1702.03348.

[19] M. H. Hamidian, S. D. Edkins, C. K. Kim, J. C. Davis, A. P. Mackenzie, H. Eisaki, S. Uchida, M. J. Lawler, E.-A. Kim, S. Sachdev, and K. Fujita, Atomic-scale electronic structure of the cuprate d-symmetry form factor density wave state, Nature Phys. **12**, 150 (2016).

[20] S. Sachdev and R. L. Placa, Bond Order in Two-Dimensional Metals with Antiferromagnetic Exchange Interactions, Phys. Rev. Lett. **111**, 027202 (2013).

[21] K. B. Efetov, H. Meier, and C. Pepin, Pseudogap state near a quantum critical point, Nature Phys. **9**, 442 (2013).

[22] L. E. Hayward, D. G Hawthorn, R. G. Melko, and S. Sachdev, Angular fluctuations of a multicomponent order describe the pseudogap of $YBa_2Cu_3O_{6+x}$, Science **343**, 1336 (2014).

[23] C. Pépin, V. S. D. Carvalho, T. Kloss, and X. Montiel, Pseudogap, charge order, and pairing density wave at the hot spots in cuprate superconductors, Phys. Rev. B **90**, 195207 (2014).

[24] E. Fradkin, S. A. Kivelson, and J. M. Tranquada, Colloquium: Theory of intertwined orders in high temperature superconductors, Rev. Mod. Phys. **87**, 457 (2015).

[25] Y. Wang, D. F. Agterberg, and A. Chubukov, Coexistence of Charge-Density-Wave and Pair-Density-Wave Orders in Underdoped Cuprates, Phys. Rev. Lett. **114**, 197001 (2015).

[26] Y. Wang, D. F. Agterberg, and A. Chubukov, Interplay between pair- and charge-density-wave orders in underdoped cuprates, Phys. Rev. B **91**, 115103 (2015).

[27] E. Fradkin and S. A. Kivelson, High-temperature superconductivity: Ineluctable complexity, Nature Phys. **8**, 864 (2012).

[28] C. V. Parker, P. Aynajian, E. H. D. S. Neto, A. Pushp, S. Ono, J. Wen, Z. Xu, G. Gu, and A. Yazdani, Fluctuating stripes at the onset of the pseudogap in the high-T(c) superconductor $Bi_2Sr_2CaCu_2O_{8+x}$, Nature (London) **468**, 677 (2010).

[29] B. Fauqué, Y. Sidis, V. Hinkov, S. Pailhès, C. T. Lin, X. Chaud, and P. Bourges, Magnetic Order in the Pseudogap Phase of High-T_C Superconductors, Phys. Rev. Lett. **96**, 197001 (2006).

[30] Y. Li, V. Balédent, N. Barišić, Y. Cho, B. Fauqué, Y. Sidis, G. Yu, X. Zhao, P. Bourges, and M. Greven, Unusual magnetic order in the pseudogap region of the superconductor $HgBa_2CuO_{4+\delta}$, Nature (London) **455**, 372 (2008).

[31] A. Shekhter, B. J. Ramshaw, R. Liang, W. N. Hardy, D. A. Bonn, F. F. Balakirev, R. D. McDonald, J. B. Betts, S. C. Riggs, and A. Migliori, Bounding the pseudogap with a line of phase transitions in $YBa_2Cu_3O_{6+\delta}$, Nature (London) **498**, 75 (2013).

[32] M. K. Chan, C. J. Dorow, L. M.-Thro, Y. Tang, Y. Ge, M. J. Veit, G. Yu, X. Zhao, A. D. Christianson, J. T. Park, Y. Sidis, P. Steffens, D. L. Abernathy, P. Bourges, and M. Greven, Commensurate antiferromagnetic excitations as a signature of the pseudogap in the tetragonal high $-$ T_c cuprate $HgBa_2CuO_{4+\delta}$, Nature Commun. **7**, 10819 (2016).

[33] L. Zhao, C. A. Belvin, R. Liang, D. A. Bonn, W. N. Hardy, N. P. Armitage, and D. Hsieh, A global inversion-symmetry-broken phase inside the pseudogap region of $YBa_2Cu_3O_y$, Nature Phys. **13**, 250 (2017).

[34] J. Corson, R. Mallozzi, J. Orenstein, J. N. Eckstein, and I. Bozovic, Vanishing of phase coherence in underdoped $Bi_2Sr_2CaCu_2O_{8+\delta}$, Nature (London) **398**, 221 (1999).

[35] Z. A. Xu, N. P. Ong, Y. Wang, T. Kakeshita, and S. Uchida, Vortex-like excitations and the onset of superconducting phase fluctuation in underdoped $La_{2-x}Sr_xCuO_4$, Nature (London) **406**, 486 (2000).

[36] K. K. Gomes, A. N. Pasupathy, A. Pushp, S. Ono, Y. Ando, and A. Yazdani, Visualizing pair formation on the atomic scale in the high-Tc superconductor $Bi_2Sr_2CaCu_2O_{8+\delta}$, Nature (London) **447**, 569 (2007).

[37] H.-B. Yang, J. D. Rameau, P. D. Johnson, T. Valla, A. Tsvelik, and G. D. Gu, Emergence of preformed Cooper pairs from the doped Mott insulating state in $Bi_2Sr_2CaCu_2O_{8+\delta}$, Nature (London) **456**, 77 (2008).

[38] A. Dubroka, M. Rössle, K. W. Kim, V. K. Malik, D. Munzar, D. N. Basov, A. A. Schafgans, S. J. Moon, C. T. Lin, D. Haug, V. Hinkov, B. Keimer, T. Wolf, J. G. Storey, J. L. Tallon, and C. Bernhard, Evidence of a Precursor Superconducting Phase at Temperatures as High as 180 K in $RBa_2Cu_3O_{7-\delta}$ (R=Y,Gd,Eu) Superconducting Crystals from Infrared Spectroscopy, Phys. Rev. Lett. **106**, 047006 (2011).

[39] L. Li, Y. Wang, M. J. Naughton, S. Ono, Y. Ando, and N. P. Ong, Strongly nonlinear magnetization above T_c in $Bi_2Sr_2CaCu_2O_{8+\delta}$, Europhys. Lett. **72**, 451 (2005).

[40] Y. Wang, L. Li, M. J. Naughton, G. D. Gu, S. Uchida, and N. P. Ong, Field-Enhanced Diamagnetism in the Pseudogap State of the Cuprate $Bi_2Sr_2CaCu_2O_{8+\delta}$ Superconductor in an Intense Magnetic Field, Phys. Rev. Lett. **95**, 247002 (2005).

[41] J. W. Cahn and J. E. Hilliard, Free energy of a nonuniform system. I. Interfacial free energy, J. Chem. Phys. **28**, 258 (1958).

[42] R. Comin and A. Damascelli, Resonant X-ray scattering studies of charge order in cuprates, Annu. Rev. Cond. Matter Phys. **7**, 369 (2016).

[43] M. Schneider, R.-S. Unger, R. Mitdank, R. Müller, A. Krapf, S. Rogaschewski, H. Dwelk, C. Janowitz, and R. Manzke, Evolution of the density of states at the Fermi level of $Bi_{2-y}Pb_ySr_{2-x}La_xCuO_{6+\delta}$ and $Bi_2Sr_{2-x}La_xCuO_{6+\delta}$ cuprates with hole doping, Phys. Rev. B **72**, 014504 (2005).

[44] S. Hüfner, M. A. Hossain, A. Damascelli, and G. A. Sawatzky, Two gaps make a high temperature superconductor? Rep. Prog. Phys. **71**, 062501 (2008).

[45] E. V. L. de Mello and J. E. Sonier, Charge segregation model for superconducting correlations in cuprates above T_c, J. Phys.: Condens. Matter **26**, 492201 (2014).

[46] S. Ono and Y. Ando, Evolution of the resistivity anisotropy in $Bi_2Sr_{2-x}La_xCuO_{6+\delta}$ single crystals for a wide range of hole doping, Phys. Rev. B **67**, 104512 (2003).

[47] K. Segawa and Y. Ando, Transport Anomalies and the Role of Pseudogap in the 60-K Phase of $YBa_2Cu_3O_{7-\delta}$, Phys. Rev. Lett. **86**, 4907 (2001).

[48] A. Yurgens, D. Winkler, T. Claeson, S. Ono, and Y. Ando, Intrinsic Tunneling Spectra of $Bi_2(Sr_{2-x}La_x)CuO_{6+\delta}$, Phys. Rev. Lett. **90**, 147005 (2003).

[49] R. Daou, J. Chang, D. LeBoeuf, O. C.-Choinière, F. Laliberté, N. D.-Leyraud, B. J. Ramshaw, R. Liang, D. A. Bonn, W. N. Hardy, and L. Taillefer, Broken rotational symmetry in the pseudogap phase of a high-T_c superconductor, Nature (London) **463**, 519 (2010).

[50] S. Vig, A. Kogar, V. Mishra, L. Venema, M. S. Rak, A. A. Husain, P. D. Johnson, G. D. Gu, E. Fradkin, M. R. Norman, and P. Abbamonte, Fluctuating charge order in the optimally doped high temperature superconductor Bi2Sr2CaCu2O8+x, arXiv:1509.04230v2.

[51] W. S. Lee, K. Vishik, I. M. and Tanaka, D. H. Lu, T. Sasagawa, N. Nagaosa, T. P. Devereaux, Z. Hussain, and Z.-X. Shen, Abrupt onset of a second energy gap at the superconducting transition of underdoped Bi2212, Nature (London) **450**, 81 (2007).

[52] T. Yoshida, M. Hashimoto, I. M. Vishik, Z.-X. Shen, and A. Fujimori, Pseudogap, superconducting gap, and fermi arc in high-T_c cuprates revealed by angle-resolved photoemission spectroscopy, J. Phys. Soc. Jpn **81**, 011006 (2012).

[53] B. Keimer, S. A. Kivelson, M. R. Norman, S. Uchida, and J. Zaanen, From quantum matter to high-temperature superconductivity in copper oxides, Nature (London) **518**, 179 (2015).

[54] B. I. Spivak and S. A. Kivelson, Negative local superfluid densities: The difference between dirty superconductors and dirty Bose liquids, Phys. Rev. B **43**, 3740 (1991).

[55] E. V. L. de Mello, Disordered-based theory of pseudogap, superconducting gap, and Fermi arc of cuprates, Europhys. Lett. **99**, 37003 (2012).

[56] D. H. Torchinsky, F. Mahmood, A. T. Bollinger, I. Božović, and N. Gedik, Fluctuating charge-density waves in a cuprate superconductor, Nature Mater. **12**, 387 (2013).

[57] A. J. Bray, Theory of phase-ordering kinetics, Adv. Phys. **43**, 357 (1994).

[58] E. V. L. D. Mello and E. S. Caixeiro, Effects of phase separation in the cuprate superconductors, Phys. Rev. B **70**, 224517 (2004).

[59] E. V. L. de Mello, R. B. Kasal, and C. A. C. Passos, Electronic phase separation transition as the origin of the superconductivity and pseudogap phase of cuprates, J. Phys.: Condens. Matter **21**, 235701 (2009).

[60] M. R. Norman, M. Randeria, H. Ding, and J. C. Campuzano, Phenomenological models for the gap anisotropy of $Bi_2Sr_2CaCu_2O_8$ as measured by angle-resolved photoemission spectroscopy, Phys. Rev. B **52**, 615 (1995).

[61] M. C. Schabel, C.-H. Park, A. Matsuura, Z.-X. Shen, D. A. Bonn, R. Liang, and W. N. Hardy, Angle-resolved photoemission on untwinned $YBa_2Cu_3O_{6.95}$. I. Electronic structure and dispersion relations of surface and bulk bands, Phys. Rev. B **57**, 6090 (1998).